Modelling and
Simulation in Materials
Science and
Engineering

PAPER

Strain-dependent transition of the relaxation dynamics in metallic glasses

To cite this article: Wenqing Zhu *et al* 2024 *Modelling Simul. Mater. Sci. Eng.* **32** 035026

IOP Publishing Modelling and Simulation in Materials Science and Engineering

Modelling Simul. Mater. Sci. Eng. **32** (2024) 035026 (23pp) https://doi.org/10.1088/1361-651X/ad29b1

Strain-dependent transition of the relaxation dynamics in metallic glasses

Wenqing Zhu[1], Yao Deng[2,3], Junjie Liu[4], Xin Yan[2,*] and Xiaoding Wei[1,5,6,*]

[1] State Key Laboratory for Turbulence and Complex System, Department of Mechanics and Engineering Science, College of Engineering, Peking University, Beijing 100871, People's Republic of China
[2] School of Mechanical Engineering and Automation, Beihang University, Beijing 100191, People's Republic of China
[3] Shanghai Highly (Group) CO., LTD, Shanghai 100124, People's Republic of China
[4] Department of Engineering Mechanics, Beijing University of Technology, Beijing 100124, People's Republic of China
[5] Beijing Innovation Center for Engineering Science and Advanced Technology, Peking University, Beijing 100871, People's Republic of China
[6] Peking University Nanchang Innovation Institute, Nanchang 330000, People's Republic of China

E-mail: yan_xin@buaa.edu.cn and xdwei@pku.edu.cn

Received 21 October 2023; revised 29 January 2024
Accepted for publication 15 February 2024
Published 4 March 2024

Abstract

Non-exponential relaxation is pervasive in glassy systems and intimately related to unique thermodynamic features, such as glass transition and aging; however, the underlying mechanisms remain unclear. The time scale of non-exponential relaxation goes beyond the time limit (nanosecond) of classic molecular dynamics simulation. Thus, the advanced time scaling atomistic approach is necessary to interpret the relaxation mechanisms at the experimental timescale. Here, we adopted autonomous basin climbing (ABC) to evaluate the long-time stress relaxation. At the same time, based on the energy minimization principle, we carried out simulations at continuum levels on the long-time stress relaxation kinetics of Cu–Zr metallic glass over timescales greater than 100 s. Combined with atomistic and continuum models, we demonstrate that a strain-dependent transition from compressed to stretched exponentials would happen, consistent with recent experimental observations on metallic glasses. Further examination of the spatial and temporal correlations of stress and plastic strain reveals two predominant driving forces: the

* Authors to whom any correspondence should be addressed.

thermal energy gradient governs in the compressed regime and leads to a release of the local internal stress; in the stretched regime, the strain energy gradient rules and causes long-range structural rearrangements. The discovery of the competition between two driving forces advances our understanding of the nature of aging dynamics in disordered solids.

Keywords: metallic glasses, stress relaxation,
spatial and temporal correlations, chemical potential

Nomenclature

σ	stress tensor,
ρ	free volume ratio,
$\boldsymbol{j}$	atomic flux,
$\boldsymbol{u}$	displacement,
ε_e	elastic strain tensor,
N_p	flow direction,
ν_p	plastic flow magnitude,
J_c	plastic swelling ratio,
M	chemical potential,
Ω^*	atomic volume,
D	diffusion coefficient,
k_B	Boltzmann constant,
T	absolute temperature,
N	degradation exponent,
λ_e, μ_e	Lame constants,
γ	surface energy density,
l	characteristic length scale.

1. Introduction

Due to the unique combination of mechanical/physical properties, metallic glasses (MGs) are promising candidate materials for structural and functional applications [1, 2]. These materials have attracted tremendous attention regarding some key scientific phenomena, such as glass transition [3], aging [4, 5], and microscopic deformation [6]. All of these phenomena are overlapped with relaxation in non-equilibrium glassy systems based on the previous experimental and numerical studies [7, 8]. Non-exponential relaxation is a classic dynamics phenomenon for conventional glassy materials, including polymeric glasses, oxide glasses, molecular glasses, and MGs. The relaxation response can be described by the empirical Kohlrausch–Williams–Watts (KWW) equation $G(t) = \exp\left[(-t/\tau)^{\beta}\right]$ in which τ is the relaxation time, and β is the shape exponent [9, 10]. Intensive studies have been carried out to unveil the physical mechanism of the non-exponential relaxation dynamics [10–22], as the outcomes promote our understanding of the nature of glasses and their properties. However, several key questions regarding the relaxation mechanism remain. For example, what critical role does mechanical stress play in the structural relaxation of MGs? And how does the mechanical stress bias the atomic dynamics?

X-ray photon correlation spectroscopy (XPCS) is a powerful tool to characterize the structural rearrangements and atomic evolution in MGs. A large number of XPCS measurements

have consistently reported a compressed ($\beta > 1$) relaxation behavior for MGs under the stress-free condition [5, 23, 24], suggesting faster atomic dynamics than in Debye relaxation (where $\beta = 1$). However, another set of XPCS measurements by Das *et al* [25] on MGs subjected to *in-situ* four-point bending reported a notable increase in τ and a surprising transition from a compressed exponential to a stretched one as the applied stress increases. On the other hand, although nearly all stress relaxation tests on MGs have consistently reported stretched exponentials [18, 20, 26–29], the study by Zhao *et al* [19] discovered a decrease in β when the imposed strain in the stress relaxation tests increases.

Despite that substantial progress has been made in experiments and modeling of the relaxation dynamics, the origin of the non-exponential relaxation remains a mystery. One hypothesis, according to classical viscoelastic theories, is that the dynamic heterogeneity in the different spatial regions leads to the apparent non-exponential decay, which could be mathematically treated as the superposition of simple exponential units [20, 30, 31]. However, since these theories are primarily phenomenological, the underpinning microscopic mechanisms are unclear. For instance, it has been pointed out recently that a superposition of simple exponentials can only lead to the stretched exponentials, but not the compressed ones [5]. In addition, the size independence of the shape exponent β discovered recently contradicts the hypothesis based on the size and spatial distribution of dynamic heterogeneity [32]. Others emphasize the role of many-body effects [33] at a very local scale, yet there is still a lack of quantitative theoretical predictions and experimental evidence. On the other hand, molecular dynamics (MD) simulations have helped to illustrate several microscopic relaxation mechanisms, such as self-diffusion [34], string-like motion [35, 36], and cage breaking [37]. Recently, Wu *et al* [38] argued that a compressed relaxation ($\beta > 1$) is related to clusters of icosahedra, whereas a stretched one ($0 < \beta < 1$) is related to isolated icosahedra. These microscopic mechanisms are responsible for the fast relaxation in glassy systems within sub-nanosecond timescales ($\sim 10^{-12}$–10^{-9} s). Nonetheless, the extremely small timescales in MD simulations make it challenging to explore the atomic relaxation dynamics in experiments (typically $\sim 10^{2}$–10^{4} s). Thus, there still remain various long-time relaxation mechanisms on the experimental timescale that need to be explored.

Recently, the researchers adopted long timescale atomistic simulation to capture the rheological behavior in response to the external loading [39]. Long timescale atomistic simulation refers to a group of simulation algorithms that could provide an atomic resolution of the physical process with a description over the timescale beyond traditional MD simulation. In general, a sampling method needs to be adopted, combined with other techniques, such as transition state theory [40], nudged elastic band (NEB) method [41], etc. With the help of these techniques, researchers could explore the slow evolution process of defects in metallic and amorphous materials, such as point defect migration [42], surface nucleation of twin boundary [43], plastic deformation of nanostructure [44, 45], and amorphous creep mechanism [46]. Of course, it should be noted that there are different sampling approaches, each with some advantages and limitations. At present, there is no general method for long timescale atomistic simulations. As to which approach a specific problem should adopt, it needs to be considered on a case-by-case basis [47]. Autonomous basin climbing (ABC) was a time scaling atomistic simulation approach developed by Sidney Yip and other researchers in 2009 [48]. It was modified from metadynamics, and it can provide an insightful description of creep and plastic slip avalanches of MGs [46, 49].

In this study, we present a two-level modeling approach to address the underlying mechanisms of long timescale relaxation in Cu–Zr MG. At the atomistic level, we use ABC combined with NEBs. At the continuum level, we employ a mechanism-based viscoplastic model for MGs based on a grand canonical thermodynamic framework [50]. Both strategies discover a

consistent strain-dependent transition of the relaxation dynamics in Cu–Zr MG, whose causes are further discussed by detailed spatio-temporal correlation analyses.

2. Atomistic modeling

2.1. ABC method and atomistic modeling

The atomic Cu–Zr MG model ($10 \times 5 \times 2\ \mathrm{nm}^3$ in size) contains 5760 atoms created by melting and quenching processes (please refer to appendix C). The periodic boundary conditions were applied in the x- and z-axes, while two free surfaces in the y-axis were created by adding a vacuum layer on each side. To simulate the stress relaxation process, we first stretched the model along the x-axis until $\varepsilon_0 = 1 \times 10^{-3}$ and 5×10^{-5}, respectively, and maintained the box length in the z-axis (thus, the model was under the plane-strain condition).

The atomic configurations associated with the stress relaxation process are probed using ABC. The specific calculation process is as follows. The initial atomic Cu–Zr MG system under an applied strain is stimulated by adding a certain number of penalty on the potential energy surface (PES) of the initial system. The penalty functions in this work are in quartic form (ϕ_i in figure 1(a)). After applying every penalty, we relaxed the system using energy minimization. After a series of penalties are applied to the system, ABC samples the PES of Cu–Zr MG system and captures the atomistic configurations of the energy minimum. Then, NEB [41] approach is adopted to calculate the energy barriers between the energy minima. Finally, we use transition state theory ($\Delta t = [\nu \exp(-\Delta U/k_\mathrm{B}T)]^{-1}$ in which ΔU is the energy barrier, ν is the attempt frequency, k_B is Boltzmann constant, and T is the absolute temperature) to convert each energy barrier into the evolution time for the relevant atomic configurations. The relaxation time is calculated through summing the transition time of all successive states ordered by stress. The variation of the stress versus the state subject to the different constant strains is shown in figures 1(b) and (c). The corresponding barrier energies of the transitions follow the axile on the right-hand side. $T = 300$ K is adopted in this work. For details of the ABC simulations, please refer to appendix C. We would like to remark that the ABC sampling is on the potential energy landscape and the entropy effect on the energy surface is not considered. The temperature effect comes into the frame in transition state theory and $T = 300$ K is adopted in this work.

2.2. Relaxation dynamics and plastic deformation

In figures 1(b) and (c), at $\varepsilon_0 = 5 \times 10^{-5}$, the stress drops to zero with small energy barriers (<0.1 eV) (figure 1(b)). At $\varepsilon_0 = 1 \times 10^{-3}$, however, only a portion of stress is relaxed, and the energy barriers are large (>0.1 eV), corresponding to a much larger relaxation time (figure 1(c)). With the evolution of the stress versus time, we can plot the relaxation function $G(t)$ versus the normalized time (t is normalized by the relaxation time τ), as shown in figure 1(d) ($G(t) = [\sigma(t) - \sigma_\infty]/\Delta\sigma$; see appendix D). KWW fitting gives a compressed exponent $\beta = 1.27$ for $\varepsilon_0 = 5 \times 10^{-5}$ and a stretched exponent $\beta = 0.30$ for $\varepsilon_0 = 1 \times 10^{-3}$. Although the applied strain $\varepsilon_0 = 5 \times 10^{-5}$ is rather small, the resulting tensile stress (≈10 MPa) is notably larger than the stress fluctuation (≈4 MPa) during NPT relaxation in MD. This confirms that the response of the model is from the mechanical stress relaxation. It is noted that the atomistic data exhibit a certain fluctuation, which arises from the unpredictable sampling path and the limited sampling states. Fluctuations in data of this kind were frequently noticed in studies involving stress relaxation or creep where ABC-based time scaling atomistic simulation was employed [51, 52].

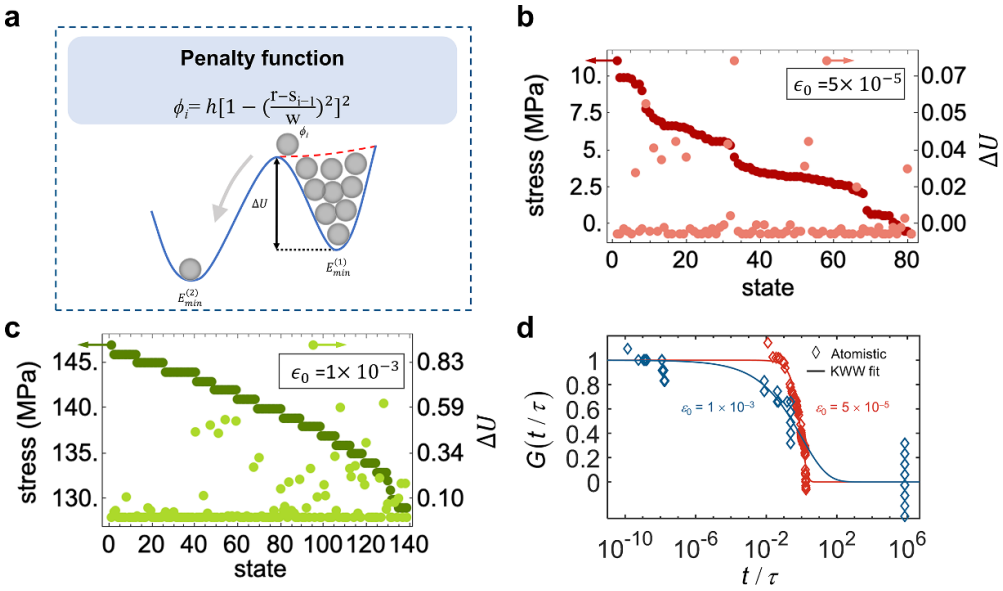

Figure 1. (a) Illustration of basin filling with quartic penalty function ϕ_i in ABC approach and the expression of the penalty function ϕ_i. Evolutions of stress and energy barrier ΔU between the successive states of Cu–Zr MG system during the relaxation processes at $\varepsilon_0 = 5 \times 10^{-5}$ (b) and $\varepsilon_0 = 1 \times 10^{-3}$ (c) sampled by ABC, respectively. (d) Relaxation function versus time at different applied strains. The solid lines are the fitted curves using the KWW equation $G(t) = \exp[(-t/\tau)^{\beta}]$.

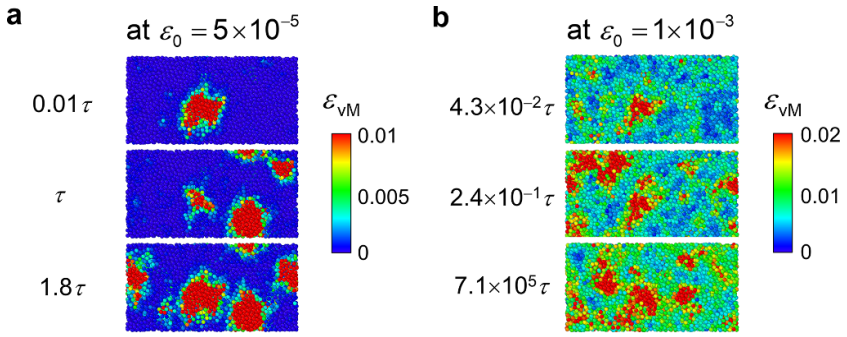

Figure 2. Typical evolutions of the local atomic plastic shear strain from ABC at $\varepsilon_0 = 5 \times 10^{-5}$ (a) and $\varepsilon_0 = 1 \times 10^{-3}$ (b).

Next, we analyze the underlying atomistic relaxation mechanism by monitoring the plastic deformation. In the compressed regime ($\varepsilon_0 = 5 \times 10^{-5}$), the isolated 'islands' of the atomic plastic strain distributes randomly inside the material (figure 2(a)). In contrast, in the stretched regime ($\varepsilon_0 = 1 \times 10^{-3}$), the plastic strain field is more uniform and becomes percolated with time increasing (figure 2(b)). It suggests that MG's relaxation dynamics and the underlying atomic motion highly depend on the mechanical strain.

3. Continuum modeling

3.1. Continuum theory and finite element modeling

In this section, we further explore the relaxation dynamics using a continuum model for the viscoplasticity of MGs, which is based on a thermodynamically consistent theoretical framework proposed in [50]. In the continuum model, the structural state of MG is represented by the spatial field of the free volume ratio, defined as $\rho(\boldsymbol{x}, t) = 1 - \Omega^* c(\boldsymbol{x}, t)$ (Ω^* is the atomic volume and c is the local atomic concentration). Note that there is a negative correlation between the change in the free volume ratio ρ and the change in the local density. A drop in ρ (i.e. $\Delta\rho < 0$) means that extra atoms are squeezed in locally so that the local free volume annihilates and the local density increases. First, a coarse-grained expression for the free energy functional of MG, Ψ, is adopted (see appendix A). Next, the initial field $\rho(\boldsymbol{x}, 0)$ is generated by an equilibrium process for the subsequent stress relaxation tests. The evolution of the free volume ratio distribution is realized through the atomic flux driven by the chemical potential gradient, $\boldsymbol{j} = -Dc \nabla \mu/k_{\mathrm{B}}T$ (μ is the chemical potential, and D is the diffusion coefficient) [53, 54]. This evolution equation guarantees a monotonic decrease in the system's free energy during the microstructural rearrangement. The whole continuum simulation algorithm is implemented in an open-source finite element method (FEM) software, FEniCS (see appendix B for details) [55, 56]. Using the above two simulation approaches, we carried out studies on the structural relaxation process and the underlying micro-mechanisms of MGs at the timescale comparable to the experiments.

FEM simulations are conducted on a 2D model (200 nm $\times$ 50 nm in size) with a mesh size of 2 nm $\times$ 2 nm. A time step of 1×10^{-3} s is used. The left end of the model was horizontally constrained, and the top and bottom edges are set as traction-free. Before the relaxation simulation, the intrinsic structural heterogeneity in the model is taken into account by assigning a random free volume ratio to each node (following a uniform distribution with the average free volume ratio $\rho_m = 0.01$ and the standard deviation of 5×10^{-3}) [57, 58] followed by an equilibration step for 10 s. The equilibration resulted in a Gaussian distribution of the free volume ratio (with the average free volume ratio $\rho_m = 0.01$ and a standard deviation of 6×10^{-4}) in the model, similar to the experimental observations [59, 60]. This equilibrated state is defined as the initial state of the system. Then, the stress relaxation tests were carried out on the model: The left end of the model was horizontally constrained, and the top and bottom edges are set as traction-free. A strain ε_0 is imposed on the right end and maintained throughout the relaxation process. The evolutions of the microstructural state and mechanical stress distribution for the MG system are obtained to perform spatio-temporal correlation analyses.

3.2. Strain-dependent transition from compressed to stretched relaxation dynamics

Thirteen relaxation tests are conducted on a 2D $Cu_{50}Zr_{50}$ sample (200×50 nm^2) subjected to an initial strain ε_0 ranging from 1.0×10^{-5}–2.0×10^{-3} using the continuum model. Figure 3(a) summarizes the relaxation processes predicted by the continuum model. Fitting the results with KWW equation to obtain the shape exponent β, we note that both simulation techniques reveal the consistent strain-dependent transition of the relaxation dynamics (figures 1(d) and 3(a)). When the imposed strain is less than a critical value (i.e. $\varepsilon_0 < \varepsilon_c \sim 1 \times 10^{-4}$),

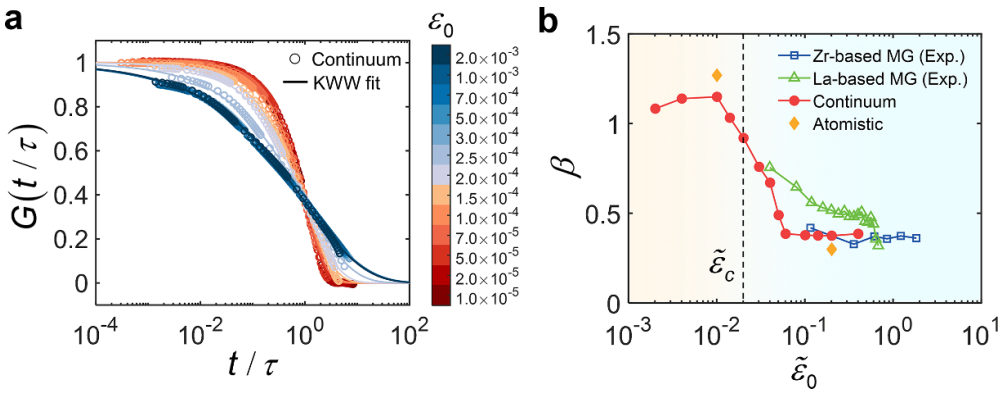

Figure 3. (a) Simulated relaxation function of MGs versus the normalized time at different applied strains based on the continuum model. The solid lines are the fitted curves using the KWW equation $G(t) = \exp[(-t/\tau)^{\beta}]$. (b) Fitted shape exponent β obtained from the continuum simulations and ABC calculation in this study compared with the previous experiments [19, 21]. The transition from the compressed exponential to the stretched exponential happens beyond the critical strain $\varepsilon_c \sim 1 \times 10^{-4}$.

the material shows a compressed relaxation ($\beta > 1$); However, when $\varepsilon_0 > \varepsilon_c$, the material shows a stretched relaxation ($\beta < 1$). The decrease in the shape exponent β with the imposed strain ε_0 agrees with the experiments on La-based and Zr-based MGs [19, 21]. The elongation of the relaxation time (see figure D1) for Zr-based MG under considerable external stress/strain has also been confirmed by recent in-situ XPCS experiments [25]. Note that $\tilde{\varepsilon}_0 = E\varepsilon_0\Omega^*/k_BT$ in figure 3(b) is the normalized imposed strain (E is Young's modulus) in order to compare our results with the previous results in the literature. The normalized critical strain where the compressed-to-stretched relaxation transition happens is $\tilde{\varepsilon}_c = 0.02$.

Moreover, the consistency between the relaxation behaviors predicted by the continuum model and ABC method indicates that the non-exponential relaxation behavior of MGs is independent of the system size—despite the diverse model sizes, a consistent change of the shape exponent β is seen. This makes us question the assumption of spatially distributed Maxwell-fluid-like regions in MGs based on the classical viscoelastic analysis: if Maxwell (simple exponential) units with the specific length scales exist in MGs, the shape exponent must exhibit size dependence. Our finding here agrees with the recent report by Shang *et al*, who also observed a scale-invariant shape exponent for binary glass models with different sizes through atomistic simulations [32].

Next, we examine the evolutions of the microstructures and microplasticity in the continuum model in two typical cases—the compressed relation at $\varepsilon_0 = 5 \times 10^{-5}$ (or the normalized strain $\tilde{\varepsilon}_0 = 0.01$), and the stretched relaxation at $\varepsilon_0 = 1 \times 10^{-3}$ (or $\tilde{\varepsilon}_0 = 0.2$). In the material after the compressed relaxation at $\tilde{\varepsilon}_0 = 0.01$, the continuum model suggests that the spatial distribution of the change of the free volume ratio (also reflecting the change of the local atomic density), $\Delta\rho$, though showing spatial fluctuations in both cases, is more scattered and random (figure D2(a)). Thus, it is not surprising that the plastic deformation, caused by the local exchange of atoms, also scattered randomly in the model (see figure 4(a)). A similar phenomenon is noticed in the ABC simulation at the normalized strain $\tilde{\varepsilon}_0 = 0.01$ (figure 2(a)). These features suggest that with a small amount of mechanical energy input, structural rearrangements happen very quickly to ease the density inhomogeneity, leading to a

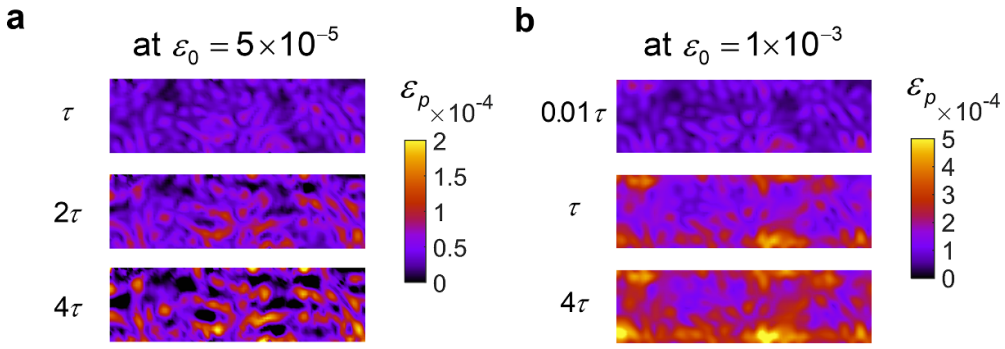

Figure 4. Typical evolutions of the plastic strain from continuum simulations at $\varepsilon_0 = 5 \times 10^{-5}$ (a) and $\varepsilon_0 = 1 \times 10^{-3}$ (b).

compressed relaxation. This short-range free volume change (or the density change) associated with a cascade mechanism of relaxation has been evidenced by the evolution of the position of the first diffraction peak through XPCS [7].

In contrast, for the model after the stretched relaxation at $\varepsilon_0 = 1 \times 10^{-3}$ (or $\tilde{\varepsilon}_0 = 0.2$), it shows that the extrema of $\Delta\rho$ occur primarily near the free surfaces of the sample (figure D2(b)), suggesting atomic dynamics gradually decaying toward the sample interior. Accordingly, the plastic deformation occurs first near the surface and then gradually 'diffuses' into the interior (figure 4(b)). Thus, the material exhibits percolated long-range plastic deformation in the stretched relaxation, compared with the isolated plastic events in the compressed relaxation (figure 4(a)). Correspondingly, ABC simulation at $\varepsilon_0 = 1 \times 10^{-3}$ gives similar plastic deformation distribution characteristics—the plastic strain field exhibits a notably larger correlation length compared with that in the small strain case (figure 2).

Despite the disparity in size between the atomistic and continuum models, they share a similar fundamental mechanism. As the applied strain increases, the strain energy density gets progressively influential, thereby impacting the evolution of the PES and the selection of microstructure evolution pathways. Thus, although the plastic strain patterns in figures 2 and 4 differ in term of their scales, the characteristic features given by both approaches for small and large applied stresses are comparable.

3.3. Spatial correlations and correlation lengths for stress and plastic strain

All the above characterizations suggest that the different relaxation dynamics in the compressed and stretched cases must be closely correlated with the distinct underlying microplasticity mechanisms. We thus examine the spatial correlation functions for the stress and plastic strain in all relaxation tests predicted by the continuum model [61, 62]:

$$C(r) = \frac{\langle s_1(0) \cdot s_2(r)\rangle - \langle s_1(0)\rangle \langle s_2(r)\rangle}{\langle s_1(0) \cdot s_2(0)\rangle - \langle s_1(0)\rangle \langle s_2(0)\rangle}, \tag{1}$$

where r is the distance from the sampled node (origin); field variables s_1 and s_2 are σ (the normal stress component) or ε_p (the plastic strain component) in the tensile direction. The representative stress autocorrelation function ($s_1 = s_2 = \sigma$) and plastic strain autocorrelation function ($s_1 = s_2 = \varepsilon_p$) for $\varepsilon_0 = 5.0 \times 10^{-5}$ and $\varepsilon_0 = 1.0 \times 10^{-3}$ are shown in figure E1. Overall, the spatial correlation functions at each moment during the relaxation consistently decay exponentially with distance. We define the correlation length ξ so that $C(\xi) = e^{-1}$. The

trends of the stress correlation length ξ_σ and the plastic strain correlation length ξ_p in all relaxation cases summarized in figures 5(a) and (b) show two distinct patterns. Despite the similar initial oscillations, ξ_σ and ξ_p in compressed relaxation cases tend to converge to the limiting length scale of our model (that is, the mesh size = 2 nm), indicating thinning stress and plastic strain networks. In contrast, in the stretched cases, ξ_σ consistently stabilizes at 3.5– 4 nm, and ξ_p stabilizes at a constant positively correlated with the applied strain ε_0. The stabilized ξ_σ and ξ_p (when $t \geqslant 4\tau$) summarized in figure 5(c) once again highlight that the change in the trends of these two correlation lengths is consistent with the transition from compressed to stretched exponentials.

More interesting features are revealed by the long-time (when $t \geqslant 4\tau$) σ–ε_p correlation functions at different applied strains in figure 5(d). When $\varepsilon_0 < 2 \times 10^{-4}$, no plausible σ–ε_p correlation is observed beyond twice the mesh size, implying short-range structural rearrangements that agree with the fine networks of ε_p distribution in figure 4(a) at $t = 4\tau$. Nevertheless, when inspecting the evolution of the Pearson correlation coefficient between σ and ε_p over time (see figure E2), we note that at small ε_0 the correlation coefficient first starts at a positive value and then gradually decays toward zero. This trend is highlighted by the $\tilde{\sigma} - \varepsilon_p$ plots in figure 5(e) for $\varepsilon_0 = 5 \times 10^{-5}$, where $\tilde{\sigma} = \sigma / (E\varepsilon_0)$ is the normal stress normalized by the initially applied mechanical stress. It is particularly worth noting that a considerable number of $\tilde{\sigma}$ values lie in the range of $2 \leqslant |\tilde{\sigma}| \leqslant 6$ at the beginning, indicating a significant internal stress distribution in the system. These internal stresses are released through short-range structural rearrangements during relaxation. This mechanism is consistent with the previous arguments for the compressed exponential relaxations—the release of the internal stress at the atomic scale causes ballistic-type motions and the cooperative atomic rearrangements [5, 7, 24, 63].

On the other hand, at large ε_0, a consistent negative $\sigma - \varepsilon_p$ correlation and negative Pearson correlation coefficient are seen throughout the relaxation procedures (see figures 5(d) and E2). These relations suggest that the accumulated plastic strain brings down the local stress in stretched cases. Taking $\varepsilon_0 = 1 \times 10^{-3}$ as an example, most of the normalized stress values at the beginning lie between 0.8 and 1.2, and exhibit a negative correlation with ε_p. The negative slope remains during the aging process (see figure 5(f)). This anti-correlation between $\tilde{\sigma}$ and ε_p at large strains agrees with the recent molecular simulations [64].

To support the findings from the 2D model, continuum simulations have also been carried out on a 3D model (see appendix F). When the applied strain increases from $\varepsilon_0 = 5 \times 10^{-5}$ to $\varepsilon_0 = 1 \times 10^{-3}$, the shape exponent β decreases from 0.93 to 0.29 (figure F1(a)). Meanwhile, the plastic strain contour transitions from an isolated distribution (figure F1(c)) to a percolated long-range pattern (figure F1(d)). This is evidenced by the increased correlation length at $\varepsilon_0 = 1 \times 10^{-3}$ (see figure F1(b)).

3.4. Effect of imposed strain on temporal correlations

Further, we examine the time correlations of the stress and plastic strain fields through the two-time correlation function [5, 25]:

$$R(t_1, t_2) = \frac{\langle s_1(t_1) \cdot s_2(t_2) \rangle - \langle s_1(t_1) \rangle \langle s_2(t_2) \rangle}{\sqrt{\left\langle [s_1(t_1) - \langle s_1(t_1) \rangle]^2 \right\rangle \left\langle [s_2(t_2) - \langle s_2(t_2) \rangle]^2 \right\rangle}}. \tag{2}$$

At small strains, the stress autocorrelation broadens subtly with time (manifested by the width perpendicular to the diagonal in figure 6(a) for the case of $\varepsilon_0 = 5 \times 10^{-5}$). However, at strains greater than ε_c, a rapid broadening of the stress autocorrelation function is seen (for example, the case of $\varepsilon_0 = 1 \times 10^{-3}$ in figure 6(b)). The broadening width of the diagonal

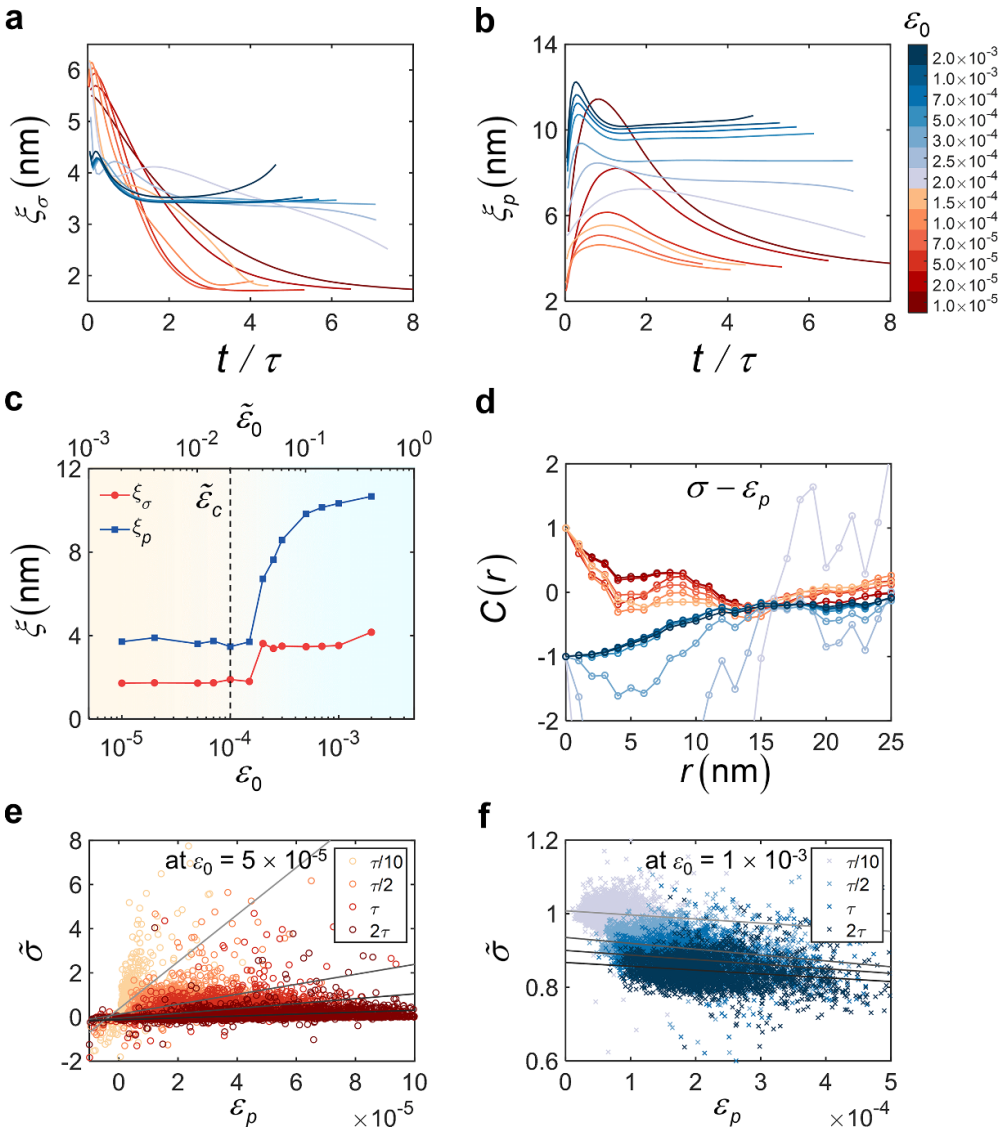

Figure 5. Effects of the applied strain on the spatial correlations. Temporal evolutions of the correlation lengths of stress autocorrelation functions (a) and plastic-strain autocorrelation functions (b) under various strains. (c) The stabilized correlation lengths ξ_σ and ξ_p vs. the applied strain. When $\varepsilon_0 < \varepsilon_c$, ξ_σ and ξ_p approach to the mesh size; however, when $\varepsilon_0 > \varepsilon_c$, these two correlation lengths enlarge (particularly ξ_p). (d) Long-time ($t \geqslant 4\tau$) σ–ε_p correlation functions at various applied strains. Evolutions of relationships of the normalized stress vs. the plastic strain at mesh nodes in the FEM model at (e) $\varepsilon_0 = 5 \times 10^{-5}$ and (f) $\varepsilon_0 = 1 \times 10^{-3}$, respectively. Solid lines are the least-squares linear fits to highlight the correlation between two variables.

intensity profile clearly shows that the application of a mechanical stress slows down the atomic dynamics in MGs. The same features have also been observed in recent XPCS experiments on the structural relaxation in MGs under external mechanical stresses [25].

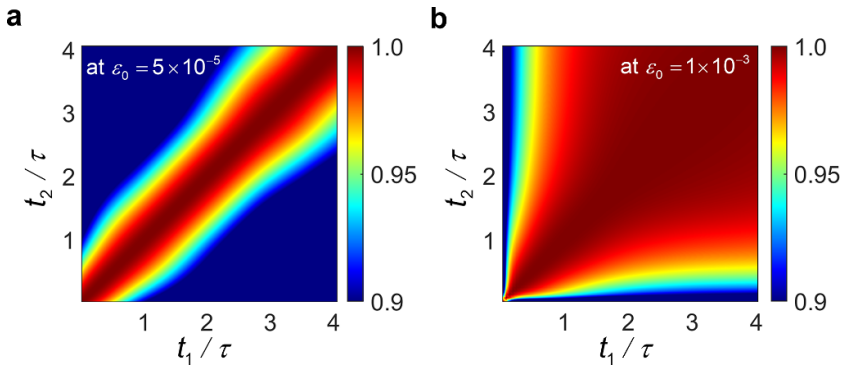

Figure 6. Two-time correlation functions under different imposed strains. Stress auto-correlation functions obtained at $\varepsilon_0 = 5 \times 10^{-5}$ (a) and $\varepsilon_0 = 1 \times 10^{-3}$ (b). Time is normalized by the relaxation time τ.

3.5. Distinct driving forces for the compressed and stretched relaxation dynamics

From the perspective of non-equilibrium thermodynamics for a dissipative system, the atomic dynamics is governed by the chemical potential gradient [33]. Thus, according to equation (A5), we express the chemical potential under the uniaxial tensile condition as

$$\mu/\Omega^* = \underbrace{2\gamma l\nabla^2\rho - \frac{2\gamma}{l}\rho + \frac{k_B T}{\Omega^*}\ln(1-\rho)}_{\text{thermal energy density}} + \underbrace{n(1-\rho)^{-1}\frac{\sigma^2}{2E} - \frac{\sigma}{3}}_{\text{elastic strain energy density}}. \tag{3}$$

The first part on the right-hand side constitutes the thermal energy portion in which the two terms are closely related to the free volume ratio ρ (or the atom density); the second part is the elastic strain energy portion. Plotting the two portions in the relaxation tests shows that the thermal part dominates at small strains, while the elastic strain energy part dominates at large strains. The change in the dominant portion of chemical potential corresponds exactly to the compressed-stretched transition of the relaxation dynamics (see figure 7(a)).

At small strains, the thermal energy part dominates so that the atomic flux $\boldsymbol{j}$ is mainly driven by $\nabla\mu$–$\nabla\rho$ (in other words, the atomic dynamics follows Fick's law. See the top snapshot in figure 7(b)). In this regime, compressed relaxation behavior is observed, and the short-range structural rearrangements help to ease the density inhomogeneities (and isolated microplasticity events), consistent with the previous XPCS studies [7].

When $\varepsilon_0 > \varepsilon_c$, the strain energy part in equation (3) begins to dominate so that the atomic flux is mainly driven by $\nabla\mu$–$\nabla\sigma$. In this regime, the relaxation is stress-driven rather than thermally driven (as shown in the bottom snapshot in figure 7(b)), and a stretched exponential is observed. Overall, the strain-dependent transition of the relaxation dynamics revealed by our continuum model and ABC simulation agree well with the recent experimental observations [7, 19, 25]. It is worth emphasizing that the driving forces for the two distinct relaxation dynamics emerged from a rigorous thermodynamics framework, and no ad-hoc empirical plastic flow rule was introduced.

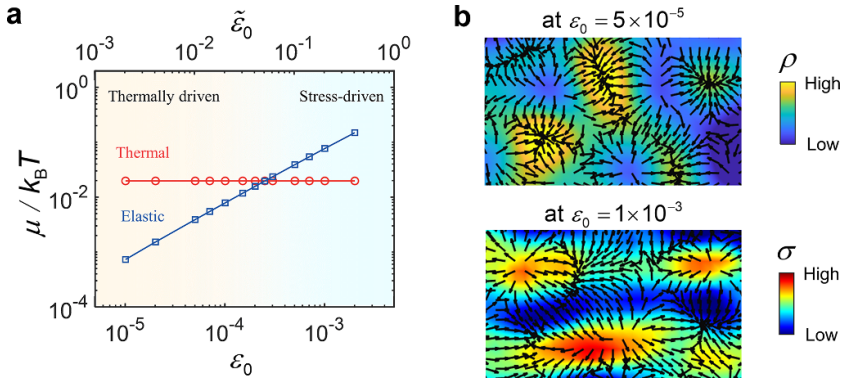

Figure 7. Thermally driven and stress-driven relaxation mechanisms in MGs. (a) Comparison of the contributions from thermal energy density and elastic strain density parts to the chemical potential. (b) Distinct atomic dynamics in the thermally driven and stress-driven relaxation processes. Top: at $\varepsilon_0 = 5 \times 10^{-5}$, the gradient of thermal energy density causes atomic flux (arrows represent the flux amplitudes as well as the directions) from 'dense' to 'loose' regions. Bottom: at $\varepsilon_0 = 1 \times 10^{-3}$, the elastic strain energy gradient drives the atoms to flow from high-stress to low-stress regions.

4. Conclusions

In this work, applying continuum mechanics theory and MD simulations, we conducted numerical modeling on MGs' relaxation dynamics on timescales comparable to those in experiments. A consistent strain-dependent transition from compressed relaxation to stretched relaxation dynamics was observed. The cause of the transition is the changes in the driving force of the relaxation dynamics. At small strains, the thermally driven atomic dynamics leads to a compressed exponential relaxation. In this regime, local structural arrangements release internal stress through dispersed plastic events. Whereas, at large strains (yet still far below the yield strain), the structural dynamics is stress-driven so that a stretched exponential is seen. In this regime, relatively long-range rearrangements are driven by the strain energy gradient, accompanied by the percolated microplasticity during the relaxation. We anticipate that the competition between stochastic local thermal forces and long-range elastic interactions commonly exists in other amorphous systems, such as yield stress fluids [65], polymer glasses [66], and granular materials [14]. Furthermore, the strain-dependent transition of the relaxation dynamics is not sensitive to the system size, suggesting that the assumption of spatially distributed fluid-like regions and the generalized Maxwell model are questionable. The findings in this study provide new insights into the micro-mechanism of relaxation dynamics in glassy materials.

Data availability statement

All data that support the findings of this study are included within the article (and any supplementary files).

Acknowledgments

We thank the support by the National Natural Science Foundation of China (Grants Nos. 12325202, 11988102 and 12372106) and by the National Key R&D Program of China (Grant No. 2020YFE0204200).

Appendix A. Mathematical framework for the continuum theory

In this study, we use the viscoplastic continuum model that was developed recently for MGs based on the laws of thermodynamics [50]. Here a brief summary of the mathematical framework is provided. After neglecting the inertia, the governing equations are summarized as:

$$\begin{cases} \text{Force balance: } \boldsymbol{\sigma}\cdot\nabla=\mathbf{0} \\ \text{Mass conservation: } \dot{\rho}-\Omega^{*}\left(\boldsymbol{j}\cdot\nabla\right)=0 \\ \text{Kinematics: } \left(\dot{\boldsymbol{u}}\nabla+\nabla\dot{\boldsymbol{u}}\right)/2=\dot{\boldsymbol{\varepsilon}}_{e}+\left[v_{p}\mathbf{N}_{p}+\dfrac{1}{3}\dot{J}_{c}\mathbf{I}\right] \\ \text{Plastic flow rule: } \mathbf{N}_{p}=\boldsymbol{\sigma}'/\left\|\boldsymbol{\sigma}'\right\|,\quad v_{p}=\Omega^{*}\left\|\left(\boldsymbol{j}\nabla\right)'\right\| \\ \text{Plastic swelling: } \dot{J}_{c}=-\Omega^{*}\boldsymbol{j}\cdot\nabla \\ \text{Microscopic kinetics: } \boldsymbol{j}=-\dfrac{D\left(1-\rho\right)}{\Omega^{*}k_{\mathrm{B}}T}\nabla\mu \\ \text{Constitutive law: } \boldsymbol{\sigma}=\dfrac{\delta\Psi}{\delta\boldsymbol{\varepsilon}_{e}}=\left(1-\rho\right)^{n}\left[\lambda_{e}\mathrm{tr}\left(\boldsymbol{\varepsilon}_{e}\right)\mathbf{I}+2\mu_{e}\boldsymbol{\varepsilon}_{e}\right] \\ \text{Chemical potential: } \mu=-\Omega^{*}\dfrac{\delta\Psi}{\delta\rho}+\dfrac{\Omega^{*}}{3}\dfrac{dJ_{c}}{d\rho}\mathrm{tr}\boldsymbol{\sigma} \\ \qquad\qquad =2\Omega^{*}\gamma l\nabla^{2}\rho-\dfrac{2\Omega^{*}\gamma}{l}\rho+k_{\mathrm{B}}T\ln\left(1-\rho\right) \\ \qquad\qquad +n\Omega^{*}\left(1-\rho\right)^{n-1}\left[\dfrac{1}{2}\lambda_{e}\mathrm{tr}\left(\boldsymbol{\varepsilon}_{e}\right)^{2}+\mu_{e}\boldsymbol{\varepsilon}_{e}:\boldsymbol{\varepsilon}_{e}\right] \\ \qquad\qquad -\dfrac{1}{3}\Omega^{*}\mathrm{tr}\boldsymbol{\sigma} \end{cases} \tag{A4}$$

where $\Psi\left(\boldsymbol{\varepsilon}_{e},\rho\right)=\int_{\Omega}\psi\left(\boldsymbol{\varepsilon}_{e},\rho,\nabla\rho\right)d\boldsymbol{r}$ is the free energy functional in which Ω is an arbitrary subregion of a system. We choose the specific form of the free energy density ψ as

$$\begin{aligned}\psi\left(\varepsilon_{e},\rho,\nabla\rho\right)=\left(1-\rho\right)^{n}\left[\frac{1}{2}\lambda_{e}\mathrm{tr}(\boldsymbol{\varepsilon}_{e})^{2}+\mu_{e}\boldsymbol{\varepsilon}_{e}:\boldsymbol{\varepsilon}_{e}\right]+\frac{k_{\mathrm{B}}T(1-\rho)}{\Omega^{*}}\left[\ln\left(1-\rho\right)-1\right]. \\ +\frac{\gamma}{l}\rho^{2}+\gamma l|\nabla\rho|^{2}\end{aligned} \tag{A5}$$

The first term on the right-hand side is the elastic energy density, where λ_e and μ_e are Lame constants; n is a degradation exponent that emerged from the power-law relationship between elastic moduli and free volume [67–69]. The second term leads to Fickian diffusion in the absence of stress [70, 71]. The last two terms stand for the gradient (interfacial) energy density ψ^{∇}. Different approaches have been proposed to formulate ψ^{∇}, including the work

by Cahn and Hilliard [72], Elder *et al* [73], and Miehe *et al* [74]. In this study, we adopt the one suggested by Miehe *et al* for phase-field fracture modeling by setting $\psi^{\nabla} = \gamma\rho^2/l + \gamma l|\nabla\rho|^2$, where the coefficient γ is the surface energy per unit area and l is a characteristic length scale (often taken as the shear band thickness). It implies an exponential spatial variation of the free volume ratio $\delta\rho \propto \exp(-|\boldsymbol{x}|/l)$ once a new interface is created [74]. These three terms constitute the thermal energy density closely related to the free volume ratio ρ (or the atom density).

Unlike the previous models that treated the amplitude of the plastic flow as a sole function of the local states, we have proposed a new approach to link the atomic kinetics with the plastic flow rationally. Both the atomic concentration and stress state contribute to the local chemical potential, whose gradient $\nabla\mu$ acts as the driving force for the atomic flux according to Einstein relation [54, 75]. Clearly, a homogenous flux will cause no macroscopic plastic deformation. Therefore, we attribute the plastic deformation to the gradient of atomic flux $\boldsymbol{j}\nabla$, which can be decomposed into two parts $\boldsymbol{j}\nabla = \frac{1}{3}(\boldsymbol{j}\cdot\nabla)\mathbf{I} + (\boldsymbol{j}\nabla)'$. Thus, the plastic strain rate is decomposed into the swelling part (related to the spherical part of $\boldsymbol{j}\nabla$, that is, $\boldsymbol{j}\cdot\nabla$ or $\dot{J}_c\mathbf{I}/3$) and the volume-conserved part (associated with the deviatoric part of $\boldsymbol{j}\nabla$, that is, $(\boldsymbol{j}\nabla)'$). The amplitude of the spherical part denotes the change of the local atomic concentration. Particularly, $(\boldsymbol{j}\cdot\nabla) > 0$ represents the atomic flux flowing out from a subregion. The deviatoric part $(\boldsymbol{j}\nabla)'$ is connected with the plastic flow amplitude v_p by $v_p = \Omega^* \left\|(\boldsymbol{j}\nabla)'\right\|$. The flow direction parallel to the deviatoric stress tensor is consistent with most of the other continuum models for MGs [76, 77].

In this study, simulations were carried out on Cu–Zr amorphous alloys in which the following parameters were employed [78–81]: Young's modulus $E = 83.5$ GPa, Poisson's ratio $\nu = 0.391$, $\gamma = 2$ J m^{-2}, $\Omega^* = 10^{-29}$ m^3 and $l = 10$ nm (approximately the shear band thickness). D is calculated as $D = D_0\exp(-\Delta G/k_{\mathrm{B}}T)$ with $D_0 = 10^{-9}$ m s^{-2} and $\Delta G = 10^{-19}$ J; $T = 300$ K. $n = 20$ is adopted based on the experimental measurements [58, 82].

Appendix B. Finite element implementation and modeling

Based on Onsager's variational principle [83, 84], the following rate-potential functional is introduced:

$$\Pi\left(\dot{\boldsymbol{u}}, \dot{\rho}, \mu, v_p\right) = \dot{\Psi}\left(\dot{\boldsymbol{\varepsilon}}_e, \dot{\rho}, \nabla\dot{\rho}\right) - \mathrm{W}^{\mathrm{ext}} + \int_{\Omega} \mu\dot{\rho}/\Omega^* \,\mathrm{d}\boldsymbol{r} + \int_{\Omega} \boldsymbol{j}\cdot(\nabla\mu)\,\mathrm{d}\boldsymbol{r}, + \int_{\Omega} \frac{\|\boldsymbol{\sigma}'\|}{2\Omega^*\left\|(\boldsymbol{j}\nabla)'\right\|} v_p^2 \,\mathrm{d}\boldsymbol{r} \tag{B6}$$

with the mechanical power exerted by the boundary forces $\mathrm{W}^{\mathrm{ext}} = \int_{\partial\Omega_t} \bar{\boldsymbol{t}}\cdot\dot{\boldsymbol{u}}\,\mathrm{d}s$. $\delta\Pi = 0$ is equivalent to the solution of the continuum model when the corresponding kinematics, constitutive relations, and proper boundary conditions have been prescribed. With this weak formulation, finite element simulations are performed using FEniCS, an open-source platform for solving partial differential equations [55, 56]. The second-order Lagrange element was used. Newton iteration was employed to solve the nonlinear equations through MUltifrontal Massively Parallel sparse direct Solver.

Simulations were conducted on a 2D model (200 nm $\times$ 50 nm in size) with a mesh size of 2 nm $\times$ 2 nm. A time step of 1×10^{-3} s was used. The left end of the model was horizontally constrained, and the top and bottom edges were set as traction-free. Before the relaxation simulation, the intrinsic structural heterogeneity in the model was taken into account by assigning a random free volume ratio to each node (following a uniform distribution with the average free volume ratio $\rho_m = 0.01$ and the standard deviation of 5×10^{-3} [57, 58]) followed by an equilibration step for 10 s. The equilibration resulted in a Gaussian distribution of the free volume ratio (with the average free volume ratio $\rho_m = 0.01$ and a standard deviation of 6×10^{-4}) in the model, similar to the experimental observations [59, 60, 85]. This equilibrated state was defined as the initial state of the system. Then, the stress relaxation tests were carried out on the model: The left end of the model was horizontally constrained, and the top and the bottom edges were set as traction-free. A strain ε_0 is imposed on the right end and maintained throughout the relaxation process.

Appendix C. Detailed methodology of ABC simulations

The embedded-atom method potential developed by Cheng *et al* was employed in our long-timescale atomistic simulation [86]. The atomistic Cu–Zr MG system was created via a rapid quench approach with periodic boundary conditions in all directions: First, a $10 \times 5 \times 2$ nm^3 $Cu_{50}Zr_{50}$ model consisting of 5760 atoms was heated to 1800 K and held for 100 ps. Next, the model was quenched down to 1 K at a constant cooling rate of 1.2×10^{11} K s^{-1} and the isothermal–isobaric (NPT) ensemble was adopted to equilibrate the system at the temperature of 1 K. Then, a vacuum space (1 nm) was added to both ends in the y-axis to mimic two free surfaces (figure C1), while the periodic boundary conditions were kept in the x- and z-axes. Last, energy minimization was performed with the steepest descent algorithm [87]. Finally, this atomistic model was ready for the relaxation simulations.

To simulate the relaxation processes using the ABC algorithm, we pre-stretched the model along the x-axis until $\varepsilon_0 = 1 \times 10^{-3}$ and 5×10^{-5}, respectively. In ABC sampling approach, at first, the steepest descent energy minimization was performed on the current system to bring it to its nearest local energy minimum. Then, we applied the quartic penalty function ($\phi_i = h[1 - \left(\frac{\boldsymbol{r} - \boldsymbol{s}_{i-1}}{w}\right)^2]^2$) to the system to sample the PES to locate the neighboring local energy minimum [48]. In the quartic penalty expression, $\boldsymbol{r}$ is the current configuration, $\boldsymbol{s}_{i-1}$ is the minimized configuration after the previous penalty was applied, w and h are shape coefficients to define the size and shape of the penalty function. The ABC algorithm is explained as follows: (1) take the pre-stretched Cu–Zr MG system as the initial state $E_{\min}^{(1)}$, and add a penalty function on PES of the initial system; (2) perform energy minimization to check whether the system locates at a new state. (3) If it is a new local minimum, record the new state $E_{\min}^{(2)}$; otherwise, go back to step (1). (4) Repeat steps (1)–(3) until sufficient states are founded.

The ABC sampling process was terminated when the internal stress of the new state dropped to zero or the number of penalty functions applied on the PES reached 3000. The sampling results were a set of minimum structures on the PES. In principle, all the new local energy minimums outputted from the ABC sampling were taken as disordered. Thus, we sorted the sampled states according to the stress level in the loading direction. Besides, the state with higher stress than the initial state were removed. Then, we applied the NEB method [41] to calculate the value of activation energies and

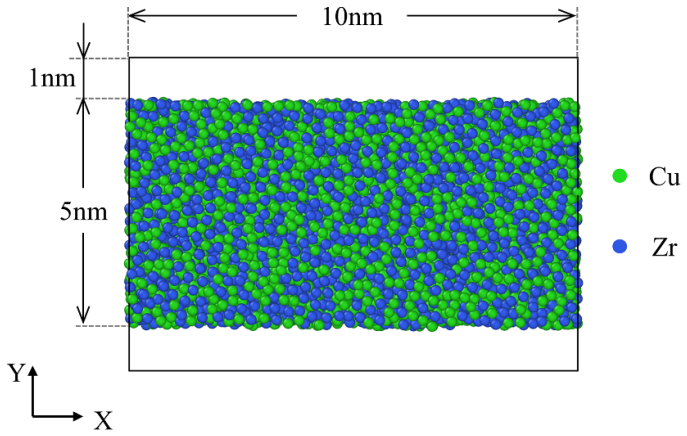

Figure C1. The initial Cu–Zr amorphous alloy structure for MD simulations.

then estimated the transition time of each evolution step through the transition-state theory. Based on the ordered sequences of the stress states, the evolution time is added up.

The atomic plastic shear strain after the relaxation was calculated using the atomic configuration right before ABC sampling as the reference configuration. The local von Mises strain representing the atom-scale plastic shear strain was evaluated as:

$$\varepsilon_{vM} = \sqrt{\varepsilon_{YZ}^2 + \varepsilon_{XZ}^2 + \varepsilon_{XY}^2 + \frac{1}{6}\left[\left(\varepsilon_{YY} - \varepsilon_{ZZ}\right)^2 + \left(\varepsilon_{XX} - \varepsilon_{ZZ}\right)^2 + \left(\varepsilon_{XX} - \varepsilon_{YY}\right)^2\right]}, \tag{C7}$$

in which ε_{ij} are the components of the local Lagrangian strain. The aforementioned algorithms were implemented in the open-source molecular dynamic code, Large-scale Atomic/Molecular Massively Parallel Simulator [88], and the Open Visualization Tool was used for visualization [89].

Appendix D. Stress relaxation results

A total of thirteen relaxation tests were carried out at imposed strains ranging from 1.0×10^{-5}–2.0×10^{-3} based on the finite element model. Long timescale atomistic simulations of stress relaxation by ABC were performed at imposed strains of 5.0×10^{-5} and 1.0×10^{-3}. During the relaxation simulation, the stress was recorded by averaging the stress over the cross-section. Figure D1 summarizes the stress *vs.* time results of all relaxation tests in which the stress is normalized by the initial value (i.e. $\tilde{\sigma}(t) = \sigma(t)/\sigma(t=0)$). The stress *vs.* time data are fitted with $R^2 > 0.97$ for all the imposed strains using KWW equation:

$$\sigma(t) = \Delta\sigma \exp\left[-(t/\tau)^{\beta}\right] + \sigma_{\infty} \tag{D8}$$

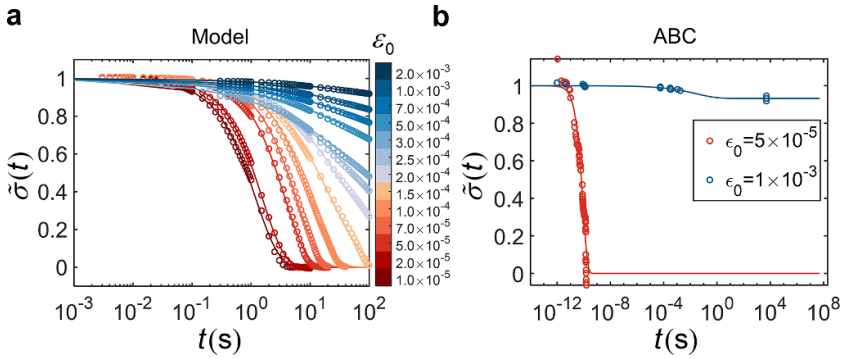

Figure D1. Normalized stress vs. time data (circles) and the curve fitting by KWW equation (solid lines) for MGs relaxation under various imposed strains for the continuum simulations (a) and ABC (b).

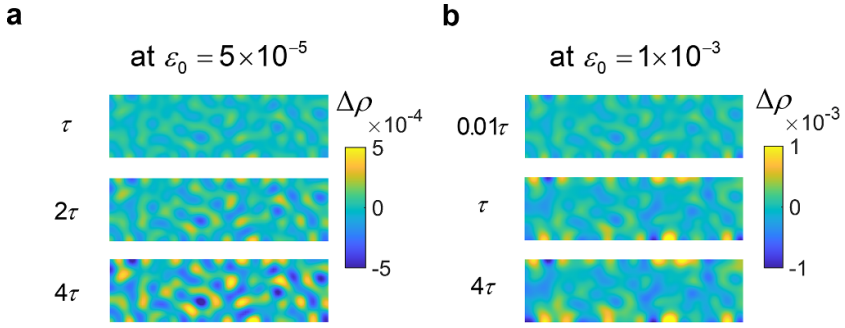

Figure D2. Typical changes of free volume ratio $\Delta\rho$ at $\varepsilon_0 = 5 \times 10^{-5}$ (a) and at $\varepsilon_0 = 1 \times 10^{-3}$ (b).

Appendix E. Spatial correlation functions

Typical spatial correlation functions of stress and plastic strain changing with time at $\varepsilon_0 = 5 \times 10^{-5}$ ($\tilde{\varepsilon}_0 = 0.01$) and 1×10^{-3} ($\tilde{\varepsilon}_0 = 0.2$) are shown in figure E1.

We also monitor the evolutions of the Pearson correlation coefficient between the stress and plastic strain at different imposed strains (see figure E2). The Pearson correlation coefficient is defined as

$$R_{\sigma-\varepsilon_p}(t) = \frac{\langle \sigma(t) \cdot \varepsilon_p(t) \rangle - \langle \sigma(t) \rangle \langle \varepsilon_p(t) \rangle}{\sqrt{\left\langle [\sigma(t) - \langle \sigma(t) \rangle]^2 \right\rangle \left\langle [\varepsilon_p(t) - \langle \varepsilon_p(t) \rangle]^2 \right\rangle}} \tag{E9}$$

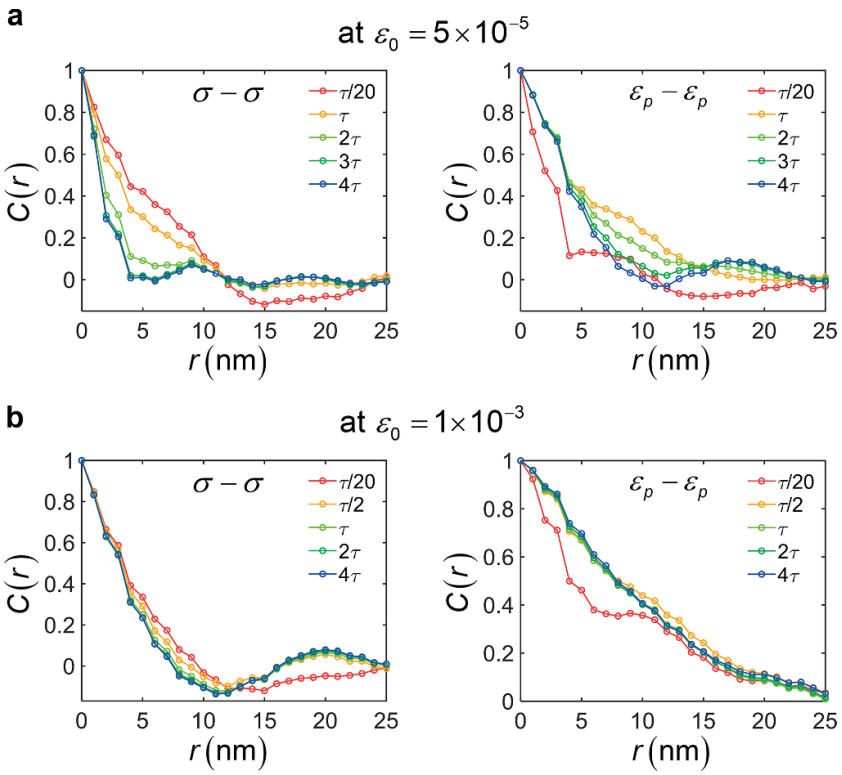

Figure E1. The spatial autocorrelation functions of stress and plastic strain at different time at $\varepsilon_0 = 5 \times 10^{-5}$ ((a) and (b)), and $\varepsilon_0 = 1 \times 10^{-3}$ ((c) and (d)), respectively.

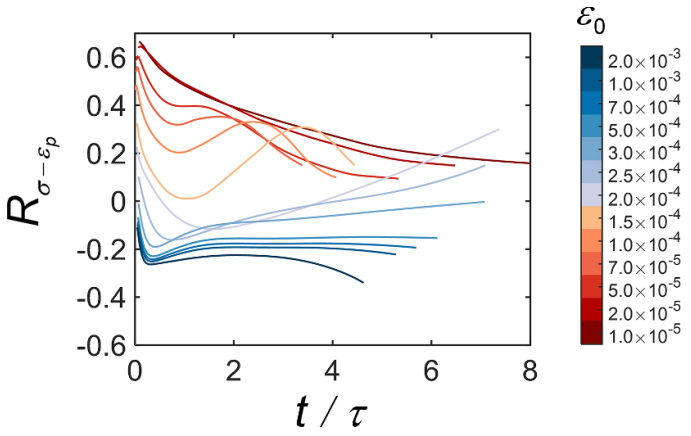

Figure E2. Evolutions of the Pearson correlation coefficient between stress and plastic strain at various imposed strains.

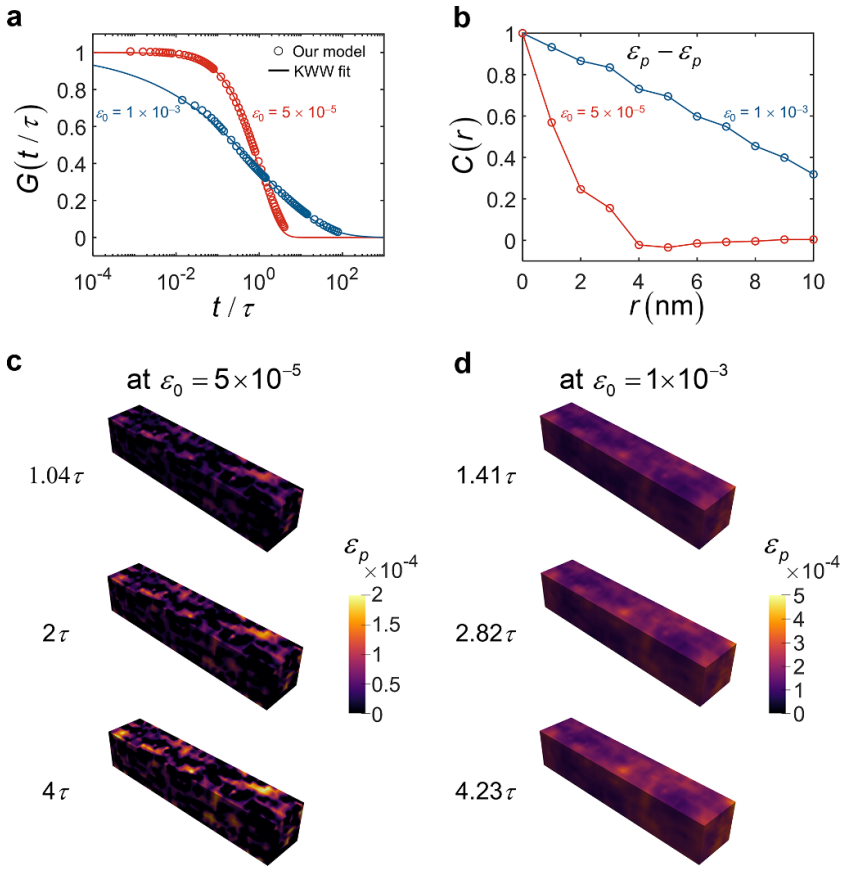

Figure F1. Transition of relaxation dynamics in 3D continuum model depending on the applied strain. (a) Relaxation functions versus time at small and large applied strains ($\varepsilon_0 = 5 \times 10^{-5}$ and $\varepsilon_0 = 1 \times 10^{-3}$). (b) The spatial autocorrelation functions of the plastic strain at $t \approx 4\tau$. (c)–(d) Typical evolutions of the plastic strain fields at $\varepsilon_0 = 5 \times 10^{-5}$ and $\varepsilon_0 = 1 \times 10^{-3}$.

Appendix F. 3D continuum model simulations

FEM simulations are also conducted on a 3D model (100 nm × 20 nm × 20 nm in size) with a mesh size of 2 nm × 2 nm × 2 nm. A time step of 1×10^{-3} s is used. Before conducting the relaxation simulation, we introduce the inherent structural heterogeneity to the model by assigning a random free volume ratio to each node. The random free volume ratio values follow a uniform distribution with an average free volume ratio $\rho_m = 0.01$ and a standard deviation of 5×10^{-3}. Subsequently, the model was equilibrated for 10 s to allow the free volume distribution stabilize. Then, the stress relaxation tests were carried out on the model: The left end of the model was horizontally constrained, and the top and bottom edges are set as traction-free. Two initial strains ($\varepsilon_0 = 5 \times 10^{-5}$ and 1×10^{-3}) are applied to the model and maintained throughout the relaxation process. Figure F1 shows the stress relaxation results and the plastic strain distribution.

ORCID iD

Xiaoding Wei https://orcid.org/0000-0002-5173-4923

References

[1] Zhou W H, Duan F H, Meng Y H, Zheng C C, Chen H M, Huang A G, Wang Y X and Li Y 2021 Effect of alloying oxygen on the microstructure and mechanical properties of Zr-based bulk metallic glass *Acta Mater.* **220** 117345
[2] Pei C, Chen S, Zhao T, Li M, Cui Z, Sun B, Hu S, Lan S, Hahn H and Feng T 2022 Nanostructured metallic glass in a highly upgraded energy state contributing to efficient catalytic performance *Adv. Mater.* **34** e2200850
[3] Hu Y-C and Tanaka H 2020 Physical origin of glass formation from multicomponent systems *Sci. Adv.* **6** eabd2928
[4] Ramos L and Cipelletti L 2005 Intrinsic aging and effective viscosity in the slow dynamics of a soft glass with tunable elasticity *Phys. Rev. Lett.* **94** 158301
[5] Ruta B, Chushkin Y, Monaco G, Cipelletti L, Pineda E, Bruna P, Giordano V M and Gonzalez-Silveira M 2012 Atomic-scale relaxation dynamics and aging in a metallic glass probed by x-ray photon correlation spectroscopy *Phys. Rev. Lett.* **109** 165701
[6] Xie X, Lo Y-C, Tong Y, Qiao J, Wang G, Ogata S, Qi H, Dahmen K A, Gao Y and Liaw P K 2019 Origin of serrated flow in bulk metallic glasses *J. Mech. Phys. Solids* **124** 634–42
[7] Giordano V M and Ruta B 2016 Unveiling the structural arrangements responsible for the atomic dynamics in metallic glasses during physical aging *Nat. Commun.* **7** 10344
[8] Fan Y, Iwashita T and Egami T 2017 Energy landscape-driven non-equilibrium evolution of inherent structure in disordered material *Nat. Commun.* **8** 15417
[9] Phillips J C 1996 Stretched exponential relaxation in molecular and electronic glasses *Rep. Prog. Phys.* **59** 1133
[10] Wang W H 2019 Dynamic relaxations and relaxation-property relationships in metallic glasses *Prog. Mater. Sci.* **106** 100589
[11] Sastry S, Debenedetti P G and Stillinger F H 1998 Signatures of distinct dynamical regimes in the energy landscape of a glass-forming liquid *Nature* **393** 554–7
[12] Ngai K 1998 Correlation between the secondary β-relaxation time at T g with the Kohlrausch exponent of the primary α relaxation or the fragility of glass-forming materials *Phys. Rev.* E **57** 7346
[13] Sturman B, Podivilov E and Gorkunov M 2003 Origin of stretched exponential relaxation for hopping-transport models *Phys. Rev. Lett.* **91** 176602
[14] Dauchot O, Marty G and Biroli G 2005 Dynamical heterogeneity close to the jamming transition in a sheared granular material *Phys. Rev. Lett.* **95** 265701
[15] Phillips J C 2011 Microscopic aspects of stretched exponential relaxation (SER) in homogeneous molecular and network glasses and polymers *J. Non-Cryst. Solids* **357** 3853–65
[16] Potuzak M, Welch R C and Mauro J C 2011 Topological origin of stretched exponential relaxation in glass *J. Chem. Phys.* **135** 214502
[17] Qiao J C and Pelletier J M 2012 Mechanical relaxation in a Zr-based bulk metallic glass: analysis based on physical models *J. Appl. Phys.* **112** 033518
[18] Wang Z, Sun B A, Bai H Y and Wang W H 2014 Evolution of hidden localized flow during glass-to-liquid transition in metallic glass *Nat. Commun.* **5** 5823
[19] Zhao L Z, Xue R J, Li Y Z, Wang W H and Bai H Y 2015 Revealing localized plastic flow in apparent elastic region before yielding in metallic glasses *J. Appl. Phys.* **118** 244901
[20] Qiao J C, Wang Y-J, Zhao L Z, Dai L H, Crespo D, Pelletier J M, Keer L M and Yao Y 2016 Transition from stress-driven to thermally activated stress relaxation in metallic glasses *Phys. Rev.* B **94** 104203
[21] Luo P, Wen P, Bai H Y, Ruta B and Wang W H 2017 Relaxation decoupling in metallic glasses at low temperatures *Phys. Rev. Lett.* **118** 225901
[22] Ngai K L 2023 Universal properties of relaxation and diffusion in complex materials: originating from fundamental physics with rich applications *Prog. Mater. Sci.* **139** 101130
[23] Ruta B, Baldi G, Monaco G and Chushkin Y 2013 Compressed correlation functions and fast aging dynamics in metallic glasses *J. Chem. Phys.* **138** 054508

[24] Evenson Z, Ruta B, Hechler S, Stolpe M, Pineda E, Gallino I and Busch R 2015 X-ray photon correlation spectroscopy reveals intermittent aging dynamics in a metallic glass *Phys. Rev. Lett.* **115** 175701
[25] Das A, Derlet P M, Liu C, Dufresne E M and Maass R 2019 Stress breaks universal aging behavior in a metallic glass *Nat. Commun.* **10** 5006
[26] Qiao J C, Wang Y-J, Pelletier J M, Keer L M, Fine M E and Yao Y 2015 Characteristics of stress relaxation kinetics of La 60 Ni 15 Al 25 bulk metallic glass *Acta Mater.* **98** 43–50
[27] Zhang C, Qiao J C, Pelletier J M and Yao Y 2016 Thermal activation in the $Zr_{65}Cu_{18}Ni_7Al_{10}$ metallic glass by creep deformation and stress relaxation *Scr. Mater.* **113** 180–4
[28] Sun B, Cao W, Wang Z, Sun B and Wang W 2022 Evident glass relaxation at room temperature induced by size effect *Phys. Rev.* B **105** 014110
[29] Sun Y T, Zhao R, Ding D W, Liu Y H, Bai H Y, Li M Z and Wang W H 2023 Distinct relaxation mechanism at room temperature in metallic glass *Nat. Commun.* **14** 540
[30] Lei T J, Rangel Dacosta L, Liu M, Wang W H, Sun Y H, Greer A L and Atzmon M 2019 Shear transformation zone analysis of anelastic relaxation of a metallic glass reveals distinct properties of α and β relaxations *Phys. Rev.* E **100** 033001
[31] Hao Q, Lyu G J, Pineda E, Pelletier J M, Wang Y J, Yang Y and Qiao J C 2022 A hierarchically correlated flow defect model for metallic glass: universal understanding of stress relaxation and creep *Int. J. Plast.* **154** 103288
[32] Shang B, Rottler J, Guan P and Barrat J L 2019 Local versus global stretched mechanical response in a supercooled liquid near the glass transition *Phys. Rev. Lett.* **122** 105501
[33] Ngai K 2011 *Relaxation and Diffusion in Complex Systems* (Springer Science & Business Media)
[34] Yu H B, Samwer K, Wu Y and Wang W H 2012 Correlation between beta relaxation and self-diffusion of the smallest constituting atoms in metallic glasses *Phys. Rev. Lett.* **109** 095508
[35] Yu H-B, Richert R and Samwer K 2017 Structural rearrangements governing Johari-Goldstein relaxations in metallic glasses *Sci. Adv.* **3** e1701577
[36] Huang B, Yuan C C, Wang Z Q, Tong Y, Wang Q, Yi J, Wang G, He Q F, Shek C H and Yang Y 2020 Influence of short- to medium-range electronic and atomic structure on secondary relaxations in metallic glasses *Acta Mater.* **196** 88–100
[37] Bi Q L, Lu Y J and Wang W H 2018 Multiscale relaxation dynamics in ultrathin metallic glass-forming films *Phys. Rev. Lett.* **120** 155501
[38] Wu Z W, Kob W, Wang W-H and Xu L 2018 Stretched and compressed exponentials in the relaxation dynamics of a metallic glass-forming melt *Nat. Commun.* **9** 1–7
[39] Cao P, Short M P and Yip S 2019 Potential energy landscape activations governing plastic flows in glass rheology *Proc. Natl Acad. Sci. USA* **116** 18790–7
[40] Nguyen L, Baker K and Warner D 2011 Atomistic predictions of dislocation nucleation with transition state theory *Phys. Rev.* B **84** 024118
[41] Henkelman G, Uberuaga B P and Jónsson H 2000 A climbing image nudged elastic band method for finding saddle points and minimum energy paths *J. Chem. Phys.* **113** 9901–4
[42] Fan Y, Yip S and Yildiz B 2014 Autonomous basin climbing method with sampling of multiple transition pathways: application to anisotropic diffusion of point defects in hcp Zr *J. Phys.: Condens. Matter* **26** 365402
[43] Tang X-Z, Zu Q and Guo Y-F 2018 The surface nucleation of tension twin via pure-shuffle mechanism: the energy landscape sampling and dynamic simulations *J. Appl. Phys.* **123** 205112
[44] Yan X and Sharma P 2016 Time-scaling in atomistics and the rate-dependent mechanical behavior of nanostructures *Nano Lett.* **16** 3487–92
[45] Tao W, Cao P and Park H S 2018 Atomistic simulation of the rate-dependent ductile-to-brittle failure transition in bicrystalline metal nanowires *Nano Lett.* **18** 1296–304
[46] Cao P, Short M P and Yip S 2017 Understanding the mechanisms of amorphous creep through molecular simulation *Proc. Natl Acad. Sci. USA* **114** 13631–6
[47] Yan X, Cao P, Tao W, Sharma P and Park H S 2016 Atomistic modeling at experimental strain rates and timescales *J. Phys. D: Appl. Phys.* **49** 493002
[48] Kushima A, Lin X, Li J, Eapen J, Mauro J C, Qian X, Diep P and Yip S 2009 Computing the viscosity of supercooled liquids *J. Chem. Phys.* **130** 224504
[49] Cao P, Dahmen K A, Kushima A, Wright W J, Park H S, Short M P and Yip S 2018 Nanomechanics of slip avalanches in amorphous plasticity *J. Mech. Phys. Solids* **114** 158–71
[50] Zhu W, Liu J, Mao S and Wei X 2021 A new continuum model for viscoplasticity in metallic glasses based on thermodynamics and its application to creep tests *J. Mech. Phys. Solids* **146** 103288

[51] Lau T T, Kushima A and Yip S 2010 Atomistic simulation of creep in a nanocrystal *Phys. Rev. Lett.* **104** 175501
[52] Tao W, Cao P and Park H S 2018 Superplastic creep of metal nanowires from rate-dependent plasticity transition *ACS Nano* **12** 4984–92
[53] Herring C 1950 Diffusional viscosity of a polycrystalline solid *J. Appl. Phys.* **21** 437–45
[54] Wei X and Kysar J W 2011 Residual plastic strain recovery driven by grain boundary diffusion in nanocrystalline thin films *Acta Mater.* **59** 3937–45
[55] Logg A, Mardal K-A and Wells G 2012 *Automated Solution of Differential Equations by the Finite Element Method: The FEniCS Book* (Springer Science & Business Media)
[56] Alnæs M S, Blechta J, Hake J, Johansson A, Kehlet B, Logg A, Richardson C, Ring J, Rognes M E and Wells G N 2015 The FEniCS project version 1.5 *Arch. Numer. Softw.* **3** 9–23
[57] Inoue A, Negishi T, HM K, Zhang T and AR Y 1998 High packing density of Zr-and Pd-based bulk amorphous alloys *Mater. Trans. JIM* **39** 318–21
[58] Chen H 1978 The influence of structural relaxation on the density and Young's modulus of metallic glasses *J. Appl. Phys.* **49** 3289–91
[59] Liu Y H, Wang D, Nakajima K, Zhang W, Hirata A, Nishi T, Inoue A and Chen M W 2011 Characterization of nanoscale mechanical heterogeneity in a metallic glass by dynamic force microscopy *Phys. Rev. Lett.* **106** 125504
[60] Ross P, Küchemann S, Derlet P M, Yu H, Arnold W, Liaw P, Samwer K and Maaß R 2017 Linking macroscopic rejuvenation to nano-elastic fluctuations in a metallic glass *Acta Mater.* **138** 111–8
[61] Cubuk ED I R, Schoenholz S S, Strickland D J, Basu A, Davidson Z S, Fontaine J, Hor J L, Huang Y R, Jiang Y and Keim N C 2017 Structure-property relationships from universal signatures of plasticity in disordered solids *Science* **358** 1033–7
[62] Wei D, Yang J, Jiang M Q, Wei B C, Wang Y J and Dai L H 2019 Revisiting the structure–property relationship of metallic glasses: common spatial correlation revealed as a hidden rule *Phys. Rev.* B **99** 014115
[63] Bouchaud J-P and Pitard E 2001 Anomalous dynamical light scattering in soft glassy gels *Eur. Phys. J.* E **6** 231–6
[64] Neudecker M and Mayr S G 2009 Dynamics of shear localization and stress relaxation in amorphous $Cu_{50}Ti_{50}$ *Acta Mater.* **57** 1437–41
[65] Coussot P, Nguyen Q D, Huynh H T and Bonn D 2002 Avalanche behavior in yield stress fluids *Phys. Rev. Lett.* **88** 175501
[66] Liu A Y H and Rottler J 2010 Aging under stress in polymer glasses *Soft Matter* **6** 4858
[67] Dederichs P, Lehmann C and Scholz A 1975 Change of elastic constants due to interstitials *Z. Phys.* B **20** 155–63
[68] Granato A 1992 Interstitialcy model for condensed matter states of face-centered-cubic metals *Phys. Rev. Lett.* **68** 974
[69] Granato A V and Khonik V A 2004 An interstitialcy theory of structural relaxation and related viscous flow of glasses *Phys. Rev. Lett.* **93** 155502
[70] Mehrer H 2007 *Diffusion in Solids: Fundamentals, Methods, Materials, Diffusion-controlled Processes* (Springer Science & Business Media)
[71] Duda F P, Ciarbonetti A, Toro S and Huespe A E 2018 A phase-field model for solute-assisted brittle fracture in elastic-plastic solids *Int. J. Plast.* **102** 16–40
[72] Cahn J W and Hilliard J E 1958 Free energy of a nonuniform system. I. Interfacial free energy *J. Chem. Phys.* **28** 258–67
[73] Elder K, Katakowski M, Haataja M and Grant M 2002 Modeling elasticity in crystal growth *Phys. Rev. Lett.* **88** 245701
[74] Miehe C, Welschinger F and Hofacker M 2010 Thermodynamically consistent phase-field models of fracture: variational principles and multi-field FE implementations *Int. J. Numer. Methods Eng.* **83** 1273–311
[75] Wei Y, Bower A and Gao H 2008 Recoverable creep deformation and transient local stress concentration due to heterogeneous grain-boundary diffusion and sliding in polycrystalline solids *J. Mech. Phys. Solids* **56** 1460–83
[76] Huang R, Suo Z, Prevost J H and Nix W D 2002 Inhomogeneous deformation in metallic glasses *J. Mech. Phys. Solids* **50** 1011–27
[77] Thamburaja P and Ekambaram R 2007 Coupled thermo-mechanical modelling of bulk-metallic glasses: theory, finite-element simulations and experimental verification *J. Mech. Phys. Solids* **55** 1236–73

[78] Johnson W L and Samwer K 2005 A universal criterion for plastic yielding of metallic glasses with a (T/Tg) 2/3 temperature dependence *Phys. Rev. Lett.* **95** 195501
[79] Zhang Y and Greer A L 2006 Thickness of shear bands in metallic glasses *Appl. Phys. Lett.* **89** 071907
[80] Greer A L, Cheng Y Q and Ma E 2013 Shear bands in metallic glasses *Mater. Sci. Eng.* R **74** 71–132
[81] Wang Y-J, Du J-P, Shinzato S, Dai L-H and Ogata S 2018 A free energy landscape perspective on the nature of collective diffusion in amorphous solids *Acta Mater.* **157** 165–73
[82] Harms U, Jin O and Schwarz R B 2003 Effects of plastic deformation on the elastic modulus and density of bulk amorphous $Pd_{40}Ni_{10}Cu_{30}P_{20}$ *J. Non-Cryst. Solids* **317** 200–5
[83] Doi M 2011 Onsager's variational principle in soft matter *J. Phys.: Condens. Matter* **23** 284118
[84] Miehe C, Hildebrand F E and Boger L 2014 Mixed variational potentials and inherent symmetries of the Cahn-Hilliard theory of diffusive phase separation *Proc. R. Soc.* A **470** 20130641
[85] Qiao J C, Zhang L T, Tong Y, Lyu G J, Hao Q and Tao K 2022 Mechancial properties of amorphous alloys: in the framework of the microstructure heterogeneity *Adv. Mech.* **52** 117–52
[86] Cheng Y, Ma E and Sheng H 2009 Atomic level structure in multicomponent bulk metallic glass *Phys. Rev. Lett.* **102** 245501
[87] Fletcher R and Powell M J 1963 A rapidly convergent descent method for minimization *Comput. J.* **6** 163–8
[88] Plimpton S 1995 Fast parallel algorithms for short-range molecular dynamics *J. Comput. Phys.* **117** 1–19
[89] Stukowski A 2009 Visualization and analysis of atomistic simulation data with OVITO–the open visualization tool *Modelling Simul. Mater. Sci. Eng.* **18** 015012